



Fast localization method of an anomaly in tissue based on differential optical density

HUIQUAN WANG,^{1,2} LINA REN,¹ ZHE ZHAO,^{1,2} JINHAI WANG,^{1,2,*} AND HONGLI CHEN^{1,2}

¹*School of Electronics and Information Engineering, Tianjin Polytechnic University, Tianjin 300387, China*

²*Tianjin Photoelectric Detection Technology and Systems Key Laboratory, Tianjin 300387, China*

*wangjinhai@tjpu.edu.cn

Abstract: The position of the source-detector (S-D) relative to an anomaly has an important influence on the detection effect in non-invasive near-infrared spectroscopy-based methods. In this study, a single-source multi-detector structure was designed in order to realize the rapid localization of anomalies within tissue. This method uses finite element analysis of the optical density distribution for different horizontal positions, depths and diameters of anomalies. The difference in optical density between the detectors was then calculated. The simulation results show that the horizontal position of the anomaly in the tissue can be quickly located according to the differential optical density difference curves formed by the multiple detectors. The Gaussian fitting feature of these curves shows strong correlation with the horizontal positions, depths and diameters of the anomaly. Through the differential optical density difference curves, rapid localization within the region of interest can be achieved. This method provides an important reference for sources and detectors location for tumor detection, brain function optical imaging and other fields using near infrared spectroscopy, and improves its detection accuracy.

© 2018 Optical Society of America under the terms of the [OSA Open Access Publishing Agreement](#)

OCIS codes: (170.6510) Spectroscopy, tissue diagnostics; (170.4580) Optical diagnostics for medicine; (170.3660) Light propagation in tissues.

References and links

1. Z. Tao, X. Dang, X. Huang, M. D. Muzumdar, E. S. Xu, N. M. Bardhan, H. Song, R. Qi, Y. Yu, T. Li, W. Wei, J. Wyckoff, M. J. Birrer, A. M. Belcher, and P. P. Ghoroghchian, "Early tumor detection afforded by in vivo imaging of near-infrared II fluorescence," *Biomaterials* **134**, 202–215 (2017).
2. R. Nosrati, K. Vesely, T. A. Schweizer, and V. Toronov, "Event-related changes of the prefrontal cortex oxygen delivery and metabolism during driving measured by hyperspectral fNIRS," *Biomed. Opt. Express* **7**(4), 1323–1335 (2016).
3. A. Kassab, J. Le Lan, P. Vannasing, and M. Sawan, "Functional near-infrared spectroscopy caps for brain activity monitoring: a review," *Appl. Opt.* **54**(3), 576–586 (2015).
4. P. Schober, S. M. Bossers, and L. A. Schwarte, "Intracranial Hematoma Detection by Near Infrared Spectroscopy in a Helicopter Emergency Medical Service: Practical Experience," *BioMed. Res. Int.* **2017**, 1–6 (2017).
5. P. A. Narayana, X. Yu, K. M. Hasan, E. A. Wilde, H. S. Levin, J. V. Hunter, E. R. Miller, V. K. S. Patel, C. S. Robertson, and J. J. McCarthy, "Multi-modal MRI of mild traumatic brain injury," *Neuroimage Clin.* **7**, 87–97 (2015).
6. D. J. Davies, Z. Su, M. T. Clancy, S. J. Lucas, H. Dehghani, A. Logan, and A. Belli, "Near-Infrared Spectroscopy in the monitoring of adult traumatic brain injury: a review," *J. Neurotrauma* **32**(13), 933–941 (2015).
7. R. Salonia, M. J. Bell, P. M. Kochanek, and R. P. Berger, "The utility of near infrared spectroscopy in detecting intracranial hemorrhage in children," *J. Neurotrauma* **29**(6), 1047–1053 (2012).
8. M. Jermyn, H. Ghadyani, M. A. Mastanduno, W. Turner, S. C. Davis, H. Dehghani, and B. W. Pogue, "Fast segmentation and high-quality three-dimensional volume mesh creation from medical images for diffuse optical tomography," *J. Biomed. Opt.* **18**(8), 086007 (2013).
9. C. S. Robertson, S. P. Gopinath, and B. Chance, "A new application for near-infrared spectroscopy: detection of delayed intracranial hematomas after head injury," *J. Neurotrauma* **12**(4), 591–600 (1995).

10. J. B. Wu, C. Shi, G. C. Chu, Q. Xu, Y. Zhang, Q. Li, J. S. Yu, H. E. Zhau, and L. W. Chung, "Near-infrared fluorescence heptamethine carbocyanine dyes mediate imaging and targeted drug delivery for human brain tumor," *Biomaterials* **67**(10), 1–10 (2015).
11. H. Tian, M. Li, Y. Wang, D. Sheng, J. Liu, and L. Zhang, "Optical wavelength selection for portable hemoglobin determination by near-infrared spectroscopy method," *Infrared Phys. Techn* **86**, 98–102 (2017).
12. M. N. Kim, B. L. Edlow, T. Durduran, S. Frangos, R. C. Mesquita, J. M. Levine, J. H. Greenberg, A. G. Yodh, and J. A. Detre, "Continuous optical monitoring of cerebral hemodynamics during head-of-bed manipulation in brain-injured adults," *Neurocrit. Care* **20**(3), 443–453 (2014).
13. X. Dai, T. Zhang, H. Yang, J. Tang, P. R. Carney, and H. Jiang, "Fast non-invasive functional diffuse optical tomography for brain imaging," *J. Biophotonics* **11**, 3 (2017).
14. J. J. Lee, D. J. Segar, J. F. Morrison, W. M. Mangham, S. Lee, and W. F. Asaad, "Subdural hematoma as a major determinant of short-term outcomes in traumatic brain injury," *J. Neurosurg.* **128**(1), 236–249 (2018).
15. L. Di Sieno, H. Wabnitz, A. Pifferi, M. Mazurenka, Y. Hoshi, A. Dalla Mora, D. Contini, G. Boso, W. Becker, F. Martelli, A. Tosi, and R. Macdonald, "Characterization of a time-resolved non-contact scanning diffuse optical imaging system exploiting fast-gated single-photon avalanche diode detection," *Rev. Sci. Instrum.* **87**(3), 035118 (2016).
16. J. Wang, D. Liu, J. Sun, Y. Zhang, Q. Sun, J. Ma, Y. Zheng, and H. Wang, "The study on increasing the equivalent SNR in the certain DOI by adjusting the SD separation in near-infrared brain imaging application," *Proc. SPIE* **157**, 101572P (2016).
17. D. Contini, L. Zucchelli, L. Spinelli, M. Caffini, R. Re, A. Pifferi, R. Cubeddu, and A. Torricelli, "Brain and muscle near infrared spectroscopy/imaging techniques," *J. Near Infrared Spectrosc.* **20**(1), 15–27 (2012).
18. C. C. Chuang, C. M. Chen, Y. S. Hsieh, T. C. Liu, and C. W. Sun, "Brain structure and spatial sensitivity profile assessing by near-infrared spectroscopy modeling based on 3D MRI data," *J. Biophotonics* **6**(3), 267–274 (2013).
19. H. Dehghani, M. E. Eames, P. K. Yalavarthy, S. C. Davis, S. Srinivasan, C. M. Carpenter, B. W. Pogue, and K. D. Paulsen, "Near infrared optical tomography using NIRFAST: Algorithm for numerical model and image reconstruction," *Commun. Numer. Methods Eng.* **25**(6), 711–732 (2009).
20. A. Hannukainen, L. Harhanen, N. Hyvönen, and H. Majander, "Edge-promoting reconstruction of absorption and diffusivity in optical tomography," *Inverse Probl.* **32**(1), 015008 (2016).
21. M. S. Wu00f3bel, A. P. Popov, A. V. Bykov, M. Kinnunen, and V. V. Tuchin, "Multi-layered tissue head phantoms for noninvasive optical diagnostics," *Journal of Innovation in Optical Health Science* **8**(03), 463–(2015).

1. Introduction

Tissue component detection methods based on near-infrared spectroscopy (NIRS) have drawn wide attention in recent years due to their rapidity and non-invasiveness. These methods have been applied in many fields such as tumor detection [1], brain imaging [2,3] and brain hematoma detection [4–7], and are gradually being applied to clinical detection. Based on multiple-source and multiple-detector patterns, using the tissue optical parameter reconstruction (Diffuse Optical Tomography, DOT) the three-dimensional distribution of the optical parameters of the tissue can be obtained in order to achieve the identification of tumors [8], hemoglobin distribution and other imaging tasks. However, these methods are computationally intensive and achieve only slow imaging speed, rendering them unsuitable for the rapid detection of anomalies. Britton Chance [9] proposed the differential Optical Density (ΔOD) method, which is based on the difference between the optical density of normal tissue and abnormal tissue. It has been fully used in brain tumors [10], tissue hemoglobin detection [11,12] and rapid cerebral hematoma detection [13,14] with good results. For example, the Infrascanner has been great clinical application in the hematoma detection. It's a simple, portable, accurate, and cost effective hematoma detection device for using in a variety of settings, including hospital emergency rooms and intensive care units. The exact placement of the source-detectors' is the key to detecting whether an anomaly exists in the target effectively [15]. The relationship between source-detectors distribution and detection results has always been a research hotspot in this field. An accurate source-detector distribution can improve tissue detection accuracy of NIRS effectively [16–18].

In this study, we used a Single-Source Multi-Detector structure (SS-MD) and utilized Nirfast's Optical Finite Element tool to construct an anomaly model with different horizontal positions, different depths and different diameters in uniform tissue [19]. We calculated the differential optical density on multiple detectors and plotted the differential optical density

difference ($\Delta OD'$) curve between adjacent detectors. Gaussian curve fitting [20] was used to fit the differential optical density difference curve, and to obtain its characteristic parameters. The experimental results show that using the differential optical density difference curve, the characteristic parameters can be used to locate anomalies in uniform tissue quickly. This method provides an additional reference for the best placement of Source-Detectors positions to detect anomalies in tissues, and the accurate positions presented will improve the near-infrared spectroscopy detection effect.

2. The differential optical density difference

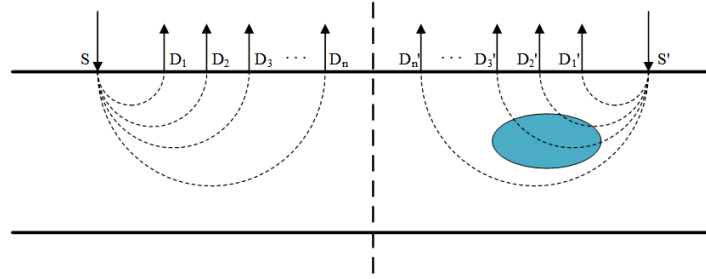


Fig. 1. Differential optical density difference curve acquisition schematic.

Figure 1 shows the differential optical density difference curve acquisition schematic. S and S' are incident sources, D_1, D_2, \dots, D_n and D_1', D_2', \dots, D_n' are equally spaced photoelectric detectors, respectively. First, we used a fixed SS-MD distribution to detect the normal tissue area. Then we used n detectors to obtain intensity measurements recorded as I_1, I_2, \dots, I_n . Second, we used the same SS-MD distribution to detect the abnormal tissue area with the same optical properties background. Then we used n detectors to obtain intensity measurements recorded as I_1', I_2', \dots, I_n' . We then obtained each position's optical density OD_1, OD_2, \dots, OD_n and $OD_1', OD_2', \dots, OD_n'$ according to the Eq. (1) and (2).

$$OD_i = \lg\left(\frac{I_0}{I_i}\right), (i = 1, 2, \dots, n) \quad (1)$$

$$OD_i' = \lg\left(\frac{I_0}{I_i'}\right), (i = 1, 2, \dots, n) \quad (2)$$

By dividing the optical density at symmetrical positions, we calculate the differential optical density.

$$\Delta OD_i = OD_i - OD_i' = \lg\frac{I_0}{I_i} - \lg\frac{I_0}{I_i'} = \lg\frac{I_i'}{I_i}, (i = 1, 2, \dots, n) \quad (3)$$

Then, we subtract the differential optical density obtained by adjacent position detectors, to find the difference of the differential optical densities at each point.

$$\Delta OD' = \Delta OD_{i+1} - \Delta OD_i, (i = 1, 2, \dots, n-1) \quad (4)$$

The multi-detector obtained $\Delta OD'$ values in turn are connected to obtain the differential optical density difference curve. This curve reflects the change rate of the optical density difference values at different S-D positions and its characteristics reflect the anomaly distribution within normal tissue.

3. Model foundation and results

In order to study the relationship between the variation trend of the differential optical density difference curve and the anomaly distribution in uniform tissue, this study used a two-dimensional uniform tissue model of 15cm*15cm based on the Nirfast optical finite element

tool, in which $\mu_a = 0.01\text{mm}^{-1}$, and $\mu_s' = 1\text{mm}^{-1}$ [21]. The model featured three kinds of Single-Source Multi-Detectors (SS-MD) distribution and was used to compare the effects of different SS-MD positions on anomaly localization. As shown in Fig. 2, for SS-MD distribution A, the source was placed at the origin, while the 10 detectors were placed equidistantly from the origin from 2cm to 10cm. SS-MD distribution B was based on distribution A, moving horizontally 2 cm to the right. Distribution C was also based on the distribution A, this time moving horizontally 4 cm to the right.

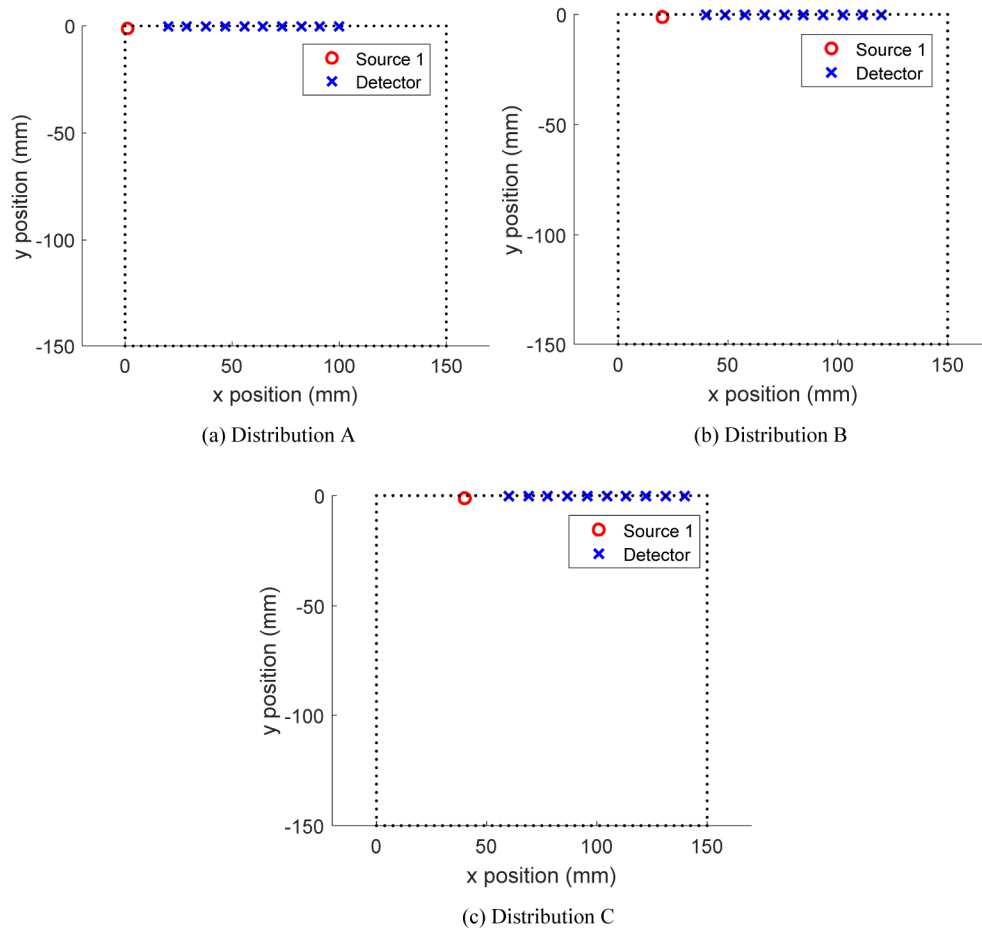


Fig. 2. Source (o) and detectors' (x) location. The coordinate system established at model vertices was used to represent the position of the source and the detectors.

3.1 Relationship between the anomaly's horizontal position and $\Delta OD'$ simulation and results

While maintaining the same depth, the anomaly's horizontal position was changed. A single anomaly was used for this experiment. The specific experimental parameters were the depth $l = 10\text{ mm}$, the diameter $d = 30\text{ mm}$, the absorption coefficient $\mu_a = 0.5\text{ mm}^{-1}$, and the scattering coefficient $\mu_s' = 1\text{ mm}^{-1}$. Then, we set the abscissa value of the anomaly to 4.0 cm, 4.5 cm, 5.0 cm, 5.5 cm, 6.0 cm, 6.5 cm, 7.0 cm, 7.5 cm, and 8.0 cm, while keeping the other parameters unchanged. The $\Delta OD'$ values measured by each detector were calculated. We selected the horizontal position of 5.0 cm, 6.0 cm, 7.0 cm as an example. Figure 3(a), (b), (c) show the relationship between the SS-MD distribution's source and detectors' distance and $\Delta OD'$ values.

Figure 3 shows that at the different detectors' positions different $\Delta OD'$ values were measured, with an obvious trend. This indicates that there is a specific relationship between the sensitivity of the $\Delta OD'$ value in the target detection zone and the source and detectors' distance. The highest $\Delta OD'$ point in the curve indicates that the differential optical density has its largest change rate at this location. The corresponding source and the detectors' distance reflects the anomaly's lateral position.

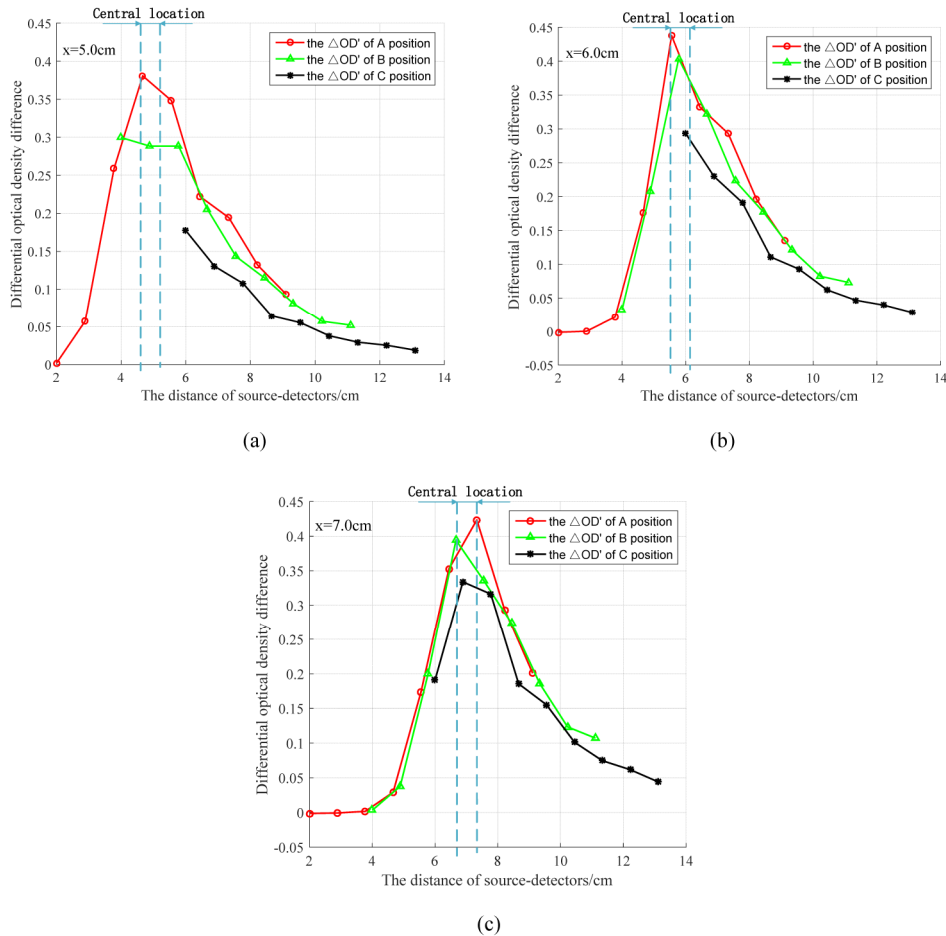


Fig. 3. $\Delta OD'$ curve of anomaly at different horizontal positions.

3.2 Relationship between the anomaly depth and $\Delta OD'$ simulation and results

In this case, the anomaly's depth was changed while maintaining the same horizontal position. The simulation parameters of the anomaly were $d = 30\text{mm}$, $\mu_a = 0.5 \text{ mm}^{-1}$, $\mu_s' = 1 \text{ mm}^{-1}$ in this experiment. The anomaly was placed 6cm from the origin in the horizontal direction. For optical brain imaging applications, the average adult scalp skull thickness is usually 1.0-1.8cm, so the anomaly's depth ranged from 1.0 to 1.8 cm at 0.1cm intervals. We then calculated the $\Delta OD'$ values measured by each detector. We selected the depths of 1.0cm, 1.2cm, 1.4cm, as examples. Figure 4(a), (b), (c) shows the relationship between the SS-MD distribution's distance and $\Delta OD'$ values; in this case, the change trend is clear as well.

This indicates that the $\Delta OD'$ value in the target detection zone was sensitive to the distance between the source and the detectors. Firstly, the distance of the anomaly to the origin in the horizontal direction was 6 cm. The maximum $\Delta OD'$ curve of the figure was also

close to 6cm, thus confirming experiment 3.1's conclusion. Meanwhile, Fig. 4 shows that the $\Delta OD'$ values were different when the depths of the anomaly were different. As the anomaly depth increases, the corresponding $\Delta OD'$ values decrease.

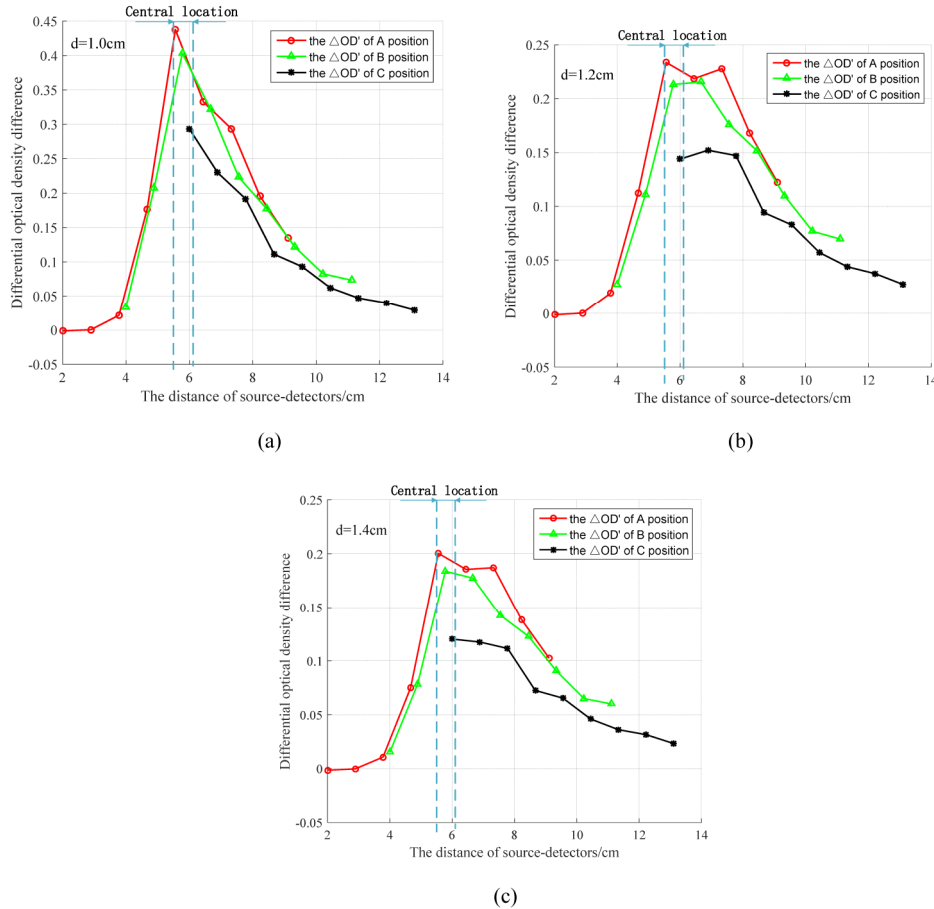


Fig. 4. The $\Delta OD'$ curve of anomaly at different depths.

3.3 Relationship between the anomaly size and $\Delta OD'$ simulation and results

For this experiment, the size of the anomaly was changed while maintaining the same horizontal position and depth. The simulation parameters of the anomaly were $l = 30\text{mm}$, $\mu_a = 0.5\text{ mm}^{-1}$, $\mu_s' = 1\text{ mm}^{-1}$ in this experiment. The anomaly was placed 7.5cm from the origin in the horizontal direction. We changed the anomaly's diameters to 1.0cm, 2.0cm, 3.0cm, 4.0cm and calculated the $\Delta OD'$ values measured by each detector. Figure 5 shows the relationship between the SS-MD distribution's distance and $\Delta OD'$ values.

Figure 5(a) shows the intensity measured by different SS-MD distributions when the anomaly was in a fixed position, confirming experiment 3.1's conclusions. The curves show the relationship between the different anomaly sizes and their corresponding $\Delta OD'$ values under the same SS-MD distribution in Fig. 5(b), (c) and (d). As can be seen from the figure, the $\Delta OD'$ value trend of each anomaly is highly similar, and as the anomaly diameters increases, their detected $\Delta OD'$ also increases.

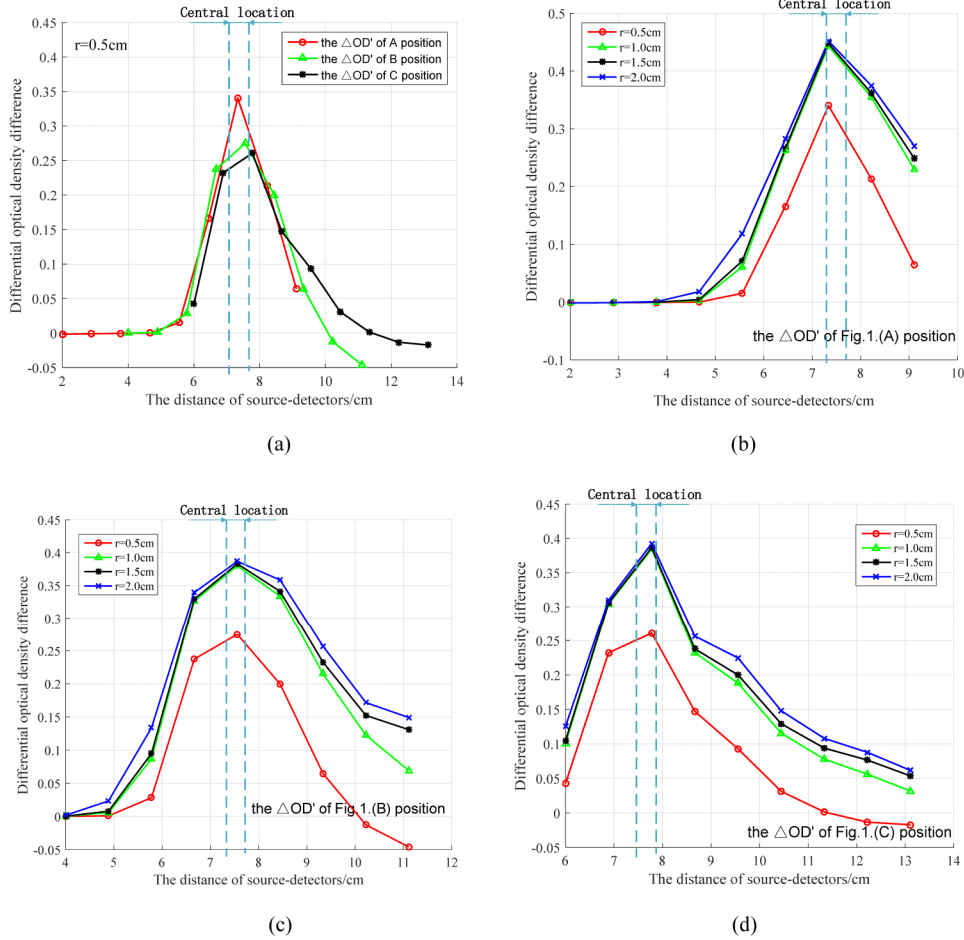


Fig. 5. $\Delta OD'$ curves of anomaly at different sizes. (a) Result of $\Delta OD'$ at $r = 0.5$ cm at different SS-MD distribution positions. (b), (c), and (d) results of $\Delta OD'$ with different sizes in fixed SS-MD positions.

4. Analysis and discussion

The spectral curves obtained in the experiment are composed of discrete points. Let these discrete data points be (x_i, y_i) . The goal of curve fitting is to find a function $y = f(x)$ between the variables x and y . The Gaussian fitting spectral curve is based on the assumption that the original spectrum is formed by stacking a number of unimodal bands. The Gaussian function system is used as the basic function of the spectral curve, that is, $y = f(x)$ is set as the Gaussian function system, where each Gaussian function is determined by three parameters: the peak height A , the peak position B , and the peak width C . The entire Gaussian function system can be written as:

$$f(x) = \sum_{i=1}^n A_i \exp\left[-\left(\frac{x - B_i}{C_i}\right)^2\right] \quad (5)$$

In the actual fitting process, we do not require $y = f(x)$ to pass through all the spectral points (x_i, y_i) , and we only require that the fitting error $(\delta = f(x) - y_i)$ on the point x_i is the smallest according to a certain criterion. This study uses the least squares method to find the best curve fit. The peak information such as peak height, peak width and peak position form a

new information matrix, which allows the extraction and simplification of the original spectral information, thus facilitating the result analysis.

$\Delta OD'$ data containing the anomaly position and size information were obtained during the simulation experiments 3.1, 3.2, and 3.3. In order to observe the variation of these discrete points more clearly, Fig. 6 used the Gaussian fitting method to extract the curve characteristic peak.

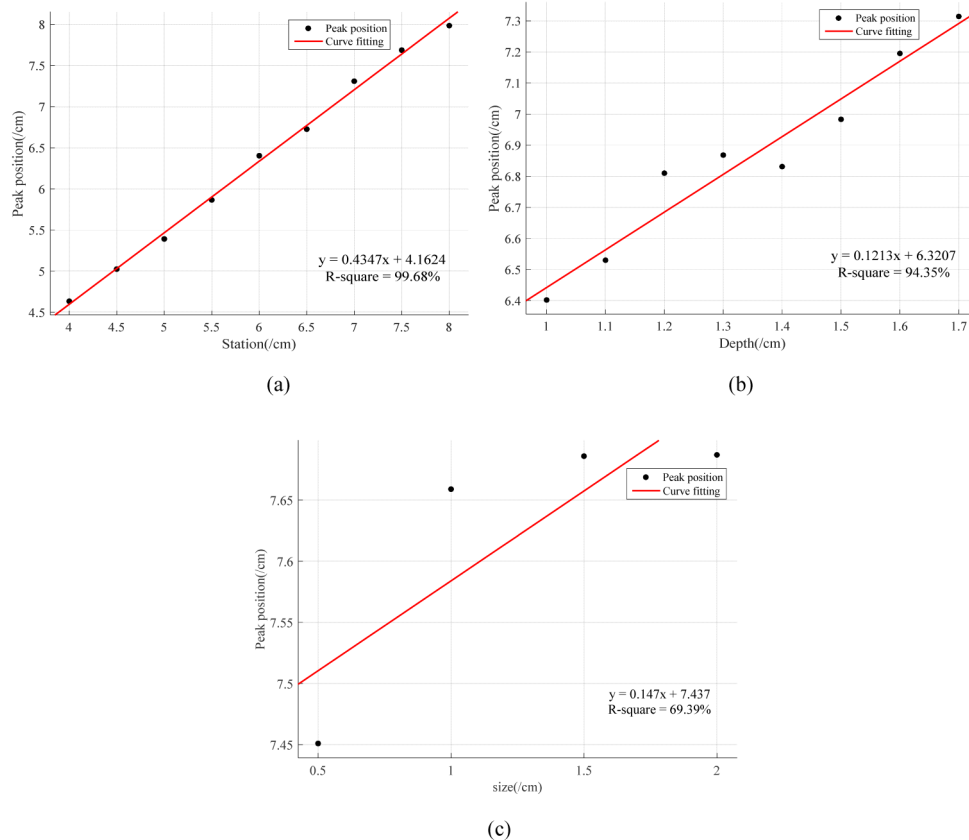


Fig. 6. Eigenvalue fitting results. (a) Curve fit of the characteristic peak about the anomaly's $\Delta OD'$ with different sizes. (b) Curve fit of the characteristic peak about the anomaly's $\Delta OD'$ at different depths. (c) Curve fit of the characteristic peak about the anomaly's $\Delta OD'$ at different positions.

As can be seen from Fig. 6(a), the characteristic peak of $\Delta OD'$ curve fit had a good correlation, 98.67% when measured with the anomaly at different horizontal positions. With the anomaly moving from left to right, the curve fitting peak was more accurate and closer to the true value when the anomaly was located in the middle of the SS-MD distribution. When the anomaly was located on either side of the SS-MD distribution, the curve peak changed within the allowable error range. As can be seen from Fig. 6(b), the characteristic peak of the $\Delta OD'$ fitting curves had a good correlation, 94.35% when measured with the anomaly at different depths. With the increase of the anomaly's depth, the peak of the $\Delta OD'$ curve fit tends to increase, and the maximum $\Delta OD'$ value can still be used to accurately represent the anomaly's presence. As can be seen from Fig. 6(c), the characteristic peak size of the $\Delta OD'$ fitted curves remains at 7.5 ± 0.2 cm, measured using anomalies of different sizes. The peak correlation was around 69% within the allowable error range. With the increase of anomaly diameters, the peak of the $\Delta OD'$ curve fit tended to increase.

The data correlation of the Gaussian curve fitting shows that the curve characteristic peaks can be used as a basis for determining whether the anomaly is present or not. This method can extract the main features of the data curves quickly and greatly simplify the original data.

5. Conclusion

This study demonstrates a method for the rapid localization of anomalies in tissues. Different SS-MD distributions were used to detect tissue-derived anomalies in unknown locations, analyze the relation between source-detectors' distance and $\Delta OD'$ values, and analyze $\Delta OD'$ trends in order to determine the anomaly's position. The results show that $\Delta OD'$ represents the sensitivity of the system to anomalies. The higher the value of $\Delta OD'$, the higher the system's sensitivity. Therefore, the proposed method can provide a reference for placing source-detector-based localization, such as tumor detection and brain function imaging. At the same time, the method can be used as an effective auxiliary means to quickly assess whether the sampled tissue contains anomalies, and also to further guide clinical screening tools.

Funding

National Natural Science Foundation of China (NSFC) (61705164).

Disclosures

The authors declare that there are no conflicts of interest related to this article.